ENGINEERING

Needle-compatible miniaturized optoelectronic sensor for pancreatic cancer detection

Seung Yup Lee[1]*, Julia M. Pakela[2,3], Kyounghwan Na[4], Jiaqi Shi[5], Barbara J. McKenna[5], Diane M. Simeone[6†], Euisik Yoon[1,4], James M. Scheiman[7‡], Mary-Ann Mycek[1,2,8§]

Pancreatic cancer is one of the deadliest cancers, with a 5-year survival rate of <10%. The current approach to confirming a tissue diagnosis, endoscopic ultrasound-guided fine-needle aspiration (EUS-FNA), requires a time-consuming, qualitative cytology analysis and may be limited because of sampling error. We designed and engineered a miniaturized optoelectronic sensor to assist in situ, real-time, and objective evaluation of human pancreatic tissues during EUS-FNA. A proof-of-concept prototype sensor, compatible with a 19-gauge hollow-needle commercially available for EUS-FNA, was constructed using microsized optoelectronic chips and microfabrication techniques to perform multisite tissue optical sensing. In our bench-top verification and pilot validation during surgery on freshly excised human pancreatic tissues (four patients), the fabricated sensors showed a comparable performance to our previous fiber-based system. The flexibility in source-detector configuration using microsized chips potentially allows for various light-based sensing techniques inside a confined channel such as a hollow needle or endoscopy.

INTRODUCTION

Pancreatic ductal adenocarcinoma (PDAC) is the third leading cause of cancer death in the United States in 2019 (*1*) and is the only major cancer with a survival rate less than 10%. Pancreatic cancer deaths have been projected to double over the next 20 years and will become the second leading cause of cancer-related death by 2030 (*2*). Current diagnostic methods, including computed tomography, magnetic resonance imaging, and endoscopic ultrasound (EUS), have clinically relevant limitations in providing an accurate diagnosis either by failing to identify small lesions or by failing to accurately differentiate masses as either adenocarcinoma or chronic pancreatitis (CP) (inflammation of the pancreas) (*3*).

The challenges to accurate pathological diagnosis of suspected pancreatic neoplasm may occur because of characteristic stromal reaction with intense fibrosis associated with both PDAC and CP. This common feature notably complicates attempts to differentiate between similar-appearing lesions on imaging, even with cytological evaluation of EUS–fine-needle aspirations (EUS-FNAs), as challenges in targeting the neoplasm are problematic (*4*). In addition, EUS-FNA suffers from low cellularity, leading to multiple insertions of the FNA needle with few cells to examine (*5*). Furthermore, well-differentiated tumors may provide challenges to the subjective cytological assessment.

Optical biopsy via light-based spectroscopy has been proposed as a complementary tool to EUS-FNA for minimally invasive, quantitative assessment. A multimodal approach combining diffuse reflectance and steady-state fluorescence spectroscopy has accurately distinguished malignant tissues from benign tissues in studies on freshly excised pancreatic tissues using histopathologic analysis as the gold standard (*6*–*8*). Furthermore, in a pilot study examining intact pancreas in vivo during pancreatic surgery (*9*), our group demonstrated a good agreement between in vivo and ex vivo measurements. Recently, one group has demonstrated technical feasibility of single-fiber reflectance spectroscopy during EUS-FNA procedure (*10*). Another group has also used light scattering spectroscopy with a fiber-optic probe through a hollow FNA needle during EUS evaluation of pancreatic cystic neoplasms and demonstrated 95% sensitivity (*11*). However, the fiber-optic probe delivered through the hollow FNA needles (19 or 22 gauge) only enables a single-point measurement with a very confined optical interrogation volume formed by a single fiber or dual fibers with a short source-detection separation. Accurate evaluation would require repetitive insertions of the needle and fiber, which could lengthen the overall procedure and increase the possibility of infection and/or pancreatitis.

Here, we have designed, fabricated, and validated a proof-of-concept 19-gauge (internal diameter, ~850 μm) FNA needle–compatible miniaturized optoelectronic (OE) sensor that integrates multiple sensing units, a pair of light sources [light-emitting diode (LED)], and a detector (phototransistor) for volumetric sensing. To build and test the entire sensing system, we have (i) performed engineering analysis on optical and thermal design, (ii) fabricated the microscale printed circuit board (μPCB) and assembled the LED and phototransistor chips, (iii) developed a custom electronics and graphic user interface (GUI) program, (iv) characterized optical and electrical performance of the assembled sensor, (v) verified the entire system performance in tissue-simulating liquid phantoms in comparison with a referent fiber optic–based diffuse reflectance spectroscopy (DRS) system, and (vi) validated on freshly excised pancreatic tissues during the Whipple or pancreatectomy procedure (total 24 tissue sites from four patients). The following section is structured in this order to

[1]Department of Biomedical Engineering, University of Michigan, Ann Arbor, MI 48109, USA. [2]Applied Physics Program, University of Michigan, Ann Arbor, MI 48109, USA. [3]Department of Radiation Oncology, University of Michigan, Ann Arbor, MI 48109, USA. [4]Department of Electrical Engineering and Computer Science, University of Michigan, Ann Arbor, MI 48109, USA. [5]Department of Pathology, University of Michigan, Ann Arbor, MI 48109, USA. [6]Department of Surgery, University of Michigan, Ann Arbor, MI 48109, USA. [7]Department of Internal Medicine, University of Michigan, Ann Arbor, MI 48109, USA. [8]Comprehensive Cancer Center, University of Michigan, Ann Arbor, MI 48109, USA.
*Present address: Department of Biomedical Engineering, Georgia Institute of Technology and Emory University, Atlanta, GA 30322, USA.
†Present address: Department of Surgery and Pathology, New York University Langone Health, New York, NY 10016, USA.
‡Present address: Division of Gastroenterology and Hepatology, University of Virginia, Charlottesville, VA 22908, USA.
§Corresponding author. Email: mycek@umich.edu

show the results of each step, with the exception of steps (ii) and (iii), which are described in Materials and Methods.

RESULTS

Design concept

Figure 1A illustrates the concept of multipoint optical sensing via the miniaturized OE sensor during the EUS-FNA procedure. Through a side-cut window of the FNA needle in a commercial EUS-FNA device (EchoTip ProCore HD, Cook Medical), multiple sensing units placed in a lateral direction can interrogate tissue surrounding the needle. Our OE sensor design is based on our previous studies using DRS, which demonstrated that the reflectance intensity ratio between 460 and 650 nm (R_{460}/R_{650}) has the diagnostic potential to distinguish malignant tissues from benign tissues (*6*, *12*). Differences in diffuse reflectance spectra (400 to 750 nm) measured on three different pancreatic tissue types including adenocarcinoma (PDAC), CP, and normal tissues from 105 sites in 22 patients are observable (Fig. 1B) (*8*), and the computed R_{460}/R_{650} is significantly different between three tissue types (Fig. 1C). Although these findings simplify sensor implementation using a single phototransistor and sequential illumination of two LEDs with discrete wavelengths, integrating all the components in a miniaturized form that can fit into a 19-gauge needle is challenging. Figure 1D shows a schematic of our miniaturized OE sensor compatible with the 19-gauge FNA needle. The single sensing unit consists of one phototransistor, as well as one 460-nm LED and one 650-nm LED, each located ~660 μm away from the phototransistor at each side. This distance is the same source-detection separation with our previous fiber optic–based reflectance spectroscopy system (*6*–*8*), maintaining the same penetration depth (about a few hundred micrometers in a superficial layer) for the purpose of validation. A microfabricated μPCB provides a base for microsized OE chip assembly via the deposited eutectic alloy and electrical interconnections. Despite the fact that monolithically fabricating an LED and photodetector on a single wafer is technically feasible for biomedical applications (*13*), we selected unpackaged die-level LEDs and a phototransistor available on the market to reduce the complexity and cost of the manufacturing process (*14*). Given that the dimension of one sensing unit is ~2 mm by 0.6 mm, multiple sensing units can be placed in a row inside the hollow FNA needle. An ultrasmall form factor of the sensor enables integration onto a stylet, a thin flexible guide filling a hollow channel during delivery of the needle through endoscopy and removed before FNA. This assembly strategy would permit colocalized optical sensing and FNA within the same needle. The potential clinical user scenario is described in fig. S1. Note that because the focus of this proof-of-concept study is on the technical feasibility of the miniaturized OE sensor, here, the fabricated OE sensor is directly attached to the inside of the needle rather than onto the stylet.

Optical design

The unpackaged die-level LED chips were selected for 460 nm (460DA3547, Cree) and 650 nm (C4L 12T5, Chip4Light) for their sufficient light emission with relatively low electrical power consumptions. We also choose an unpackaged phototransistor (T1090P, Vishay) with a high radiant detection efficiency and adequate sensitivity in the visible range. The feasibility of optical sensing using the selected OE components was verified computationally via the Monte Carlo (MC) embedded function available through the commercial ray-tracing software Zemax (Zemax 12). The simulation predicts that when the LED emitted 0.5 mW of angularly distributed power, the phototransistor detected a power of >3 mW/cm^2, generating a photocurrent of >50 μA. Given that the dark current of the phototransistor is 1 nA, the expected theoretical signal-to-noise ratio (SNR) is >90 dB; however, the SNR is expected to be lower as a result of additional noise sources from the custom LED driver and transimpedance amplifier (TIA). In addition, the MC simulation visualized the trajectory paths of individual photons detected by the phototransistor, as shown in Fig. 2A, representing an optical interrogation volume formed by the current source-detector geometry.

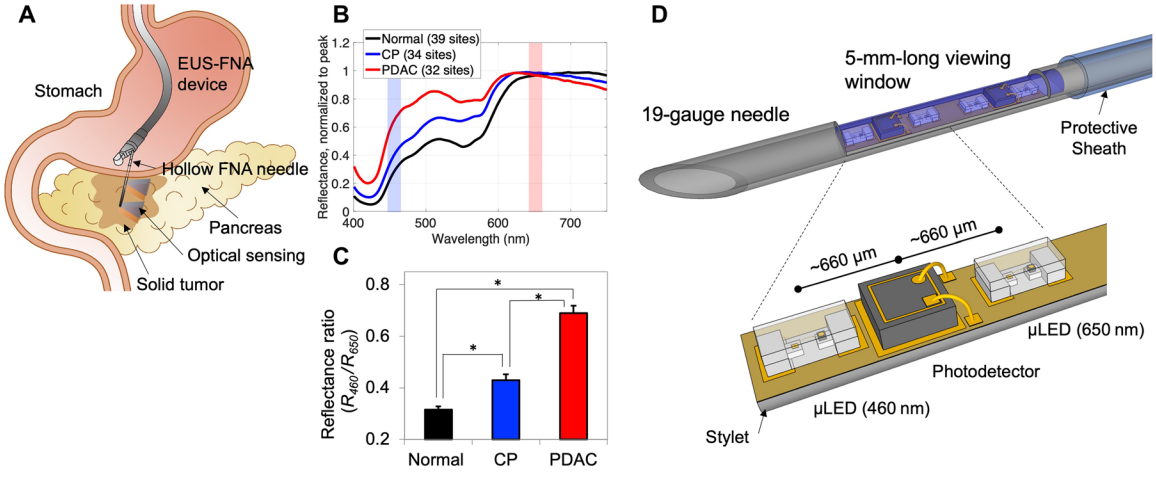

Fig. 1. Design concept of a miniaturized needle-compatible OE sensor. (**A**) Illustration depicts an application scenario of 19-gauge needle–compatible miniaturized sensor through a commercial EUS-FNA device for enlarged optical interrogation volume with multiple sensing units. (**B**) Mean normalized reflectance spectra acquired from our previous ex vivo DRS measurements on human pancreatic tissues (a total of 22 patients and 105 sites including normal tissue, CP, and PDAC) establish that the spectral shape of each tissue type is different. The wavelengths showing the maximum (blue shaded) and minimal (red shaded) difference between different tissues can be selected for a ratiometric analysis. (**C**) The reflectance ratios (R_{460}/R_{650} nm) computed from DRS are significantly different between three pancreatic tissues (*$P < 0.001$, Wilcoxon rank sum test). Error bars are SEs. (**D**) Three-dimensional (3D) design concept of the miniaturized OE sensor.

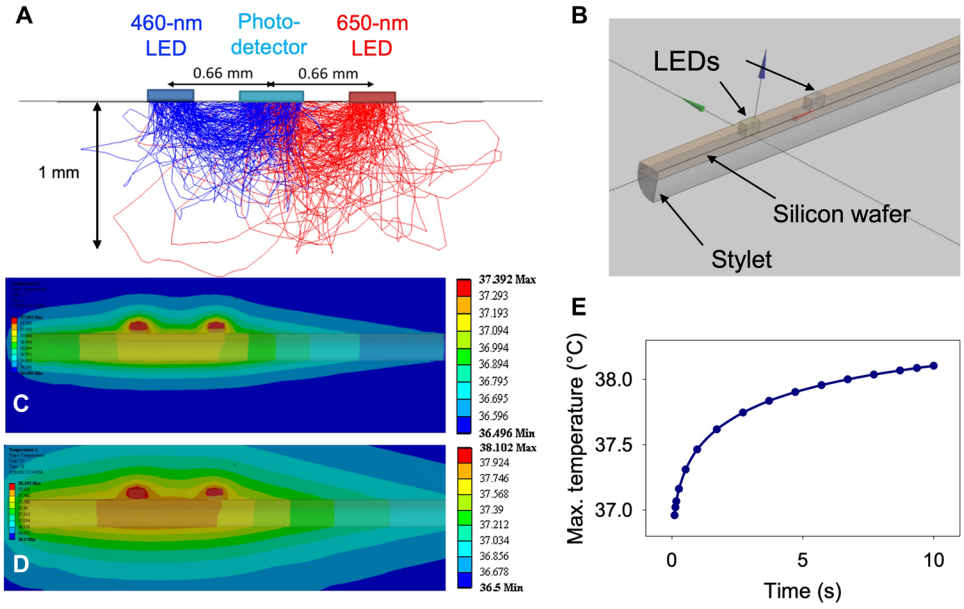

Fig. 2. Computational design analysis. Computational design tools perform engineering analysis and confirm feasibility of optical sensing and thermal safety of the miniaturized sensor. (**A**) MC simulation visualizes the path traveled by photons (blue, 460 nm; red, 650 nm) collected by the phototransistor inside a pancreatic tissue model. (**B**) 3D model of the integrated sensor for heat transfer analysis given the heat dissipation from two LEDs and the heat capacitance of each component. (**C** and **D**) Side view of temperature distribution after (C) 1 s of LED illumination and (D) in equilibrium after about 10 s shows that the maximum temperature increase is only 1° right on the LEDs and the temperature increase in adjacent pancreatic tissues is minimal. (**E**) Time series maximum temperature profile shows that the temperature stabilizes after 10 s with continuous LED illumination.

The penetration depth is roughly estimated to be ~350 and ~500 μm for 460 and 650 nm, respectively, and the total interrogation volume is estimated to be ~0.25 mm^3, assuming that the volume is a hemisphere. This estimated volume is close to the simulated volume interrogated by the fiber-optic probe used in our previous study and also comparable to the volume of a smeared tissue sample obtained during EUS-FNA.

Furthermore, we evaluated the ability to distinguish three different tissue types. The MC simulations run on the optical models of normal pancreatic tissues, CP, and PDAC at 460 and 650 nm. The LED light intensities are set to 0.6 and 0.5 mW for the 460- and 650-nm LEDs, respectively, according to their specifications. The simulated R_{460}/R_{650} are 0.76, 0.91, and 1.21 for normal pancreas, CP, and PDAC, respectively. To account for the difference in excitation intensity of the two LEDs, the R_{460}/R_{650} of PDAC is scaled to 0.71 (the averaged ratio from the experiments shown in Fig. 1C), which results in 0.44 and 0.53 for normal pancreatic tissues and CP, respectively. This result reveals that our OE sensor measuring reflectance intensity ratio at specific wavelengths can differentiate PDAC from both normal pancreas and CP. Last, to investigate the sensitivity to the environment temperature, we simulated the reflectance ratios using optical properties with wavelengths that were 5 nm longer to mimic the increased peak emission wavelength, corresponding to a temperature increase of 50°C (*15*). The simulated R_{465}/R_{655} of all three tissue types are within 1% of R_{460}/R_{650}, confirming stable optical performance of the sensor against the potential temperature variation in an in vivo tissue environment.

Thermal design

LED emission generates heat due to energy dissipation by conversion from electrical to optical power. Thus, a critical design factor is to ensure that there will be no tissue damage from heat during OE sensor operation in human pancreatic tissues. To estimate temperature changes by LED emission, heat transfer was simulated using finite element analysis implemented through Ansys software (Ansys). The sensor assembly, consisting of two LEDs located 1.2 mm apart from each other atop a silicon wafer attached on a guide stylet, was modeled using a realistic dimension and the properties related to heat transfer (Fig. 2B; see Materials and Methods). LED power was set to 1 mW (double the power used for optical simulation) operating with 10 mW of electrical power. After 1-s emission of both LEDs, the maximum temperature reaches 37.4°C (Fig. 2C). One second is a sufficiently longer time scale than our expected optical sensing time (<0.5 s) for real-time feedback. While the maximum temperature occurs inside the LED body, the maximum temperature of the surrounding pancreatic tissues is found to be around 37.0°C, less than an increase of 1°C from the initial tissue temperature of 36.5°C. In a steady-state model, temperature stabilizes in 38.1°C at 10 s, and the maximum tissue temperature is about 37.6°C (Fig. 2, D and E). It is also noted that the area with temperature changes is limited to within 5 mm around the sensor. These results demonstrate that our sensor contributes a negligible temperature increase in a very limited area and is unlikely to cause tissue damage. This simulation carries the assumption of a perfect contact between LEDs and the surrounding tissues, indicating no thermal contact resistance. In reality, the maximum tissue temperature would be further reduced.

Engineered devices

Figure 3 shows an engineered proof-of-concept prototype of a needle-compatible OE sensor. The handheld probe module (Fig. 3A) is comprised of a sensor assembly on the microfabricated μPCB, 19-gauge

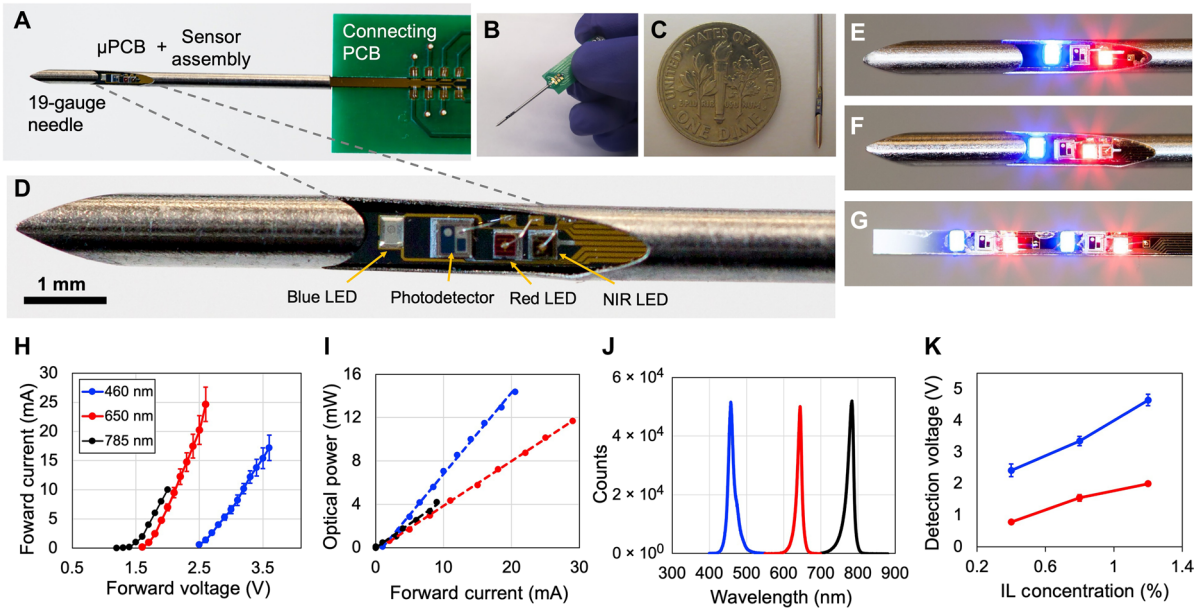

Fig. 3. Fabricated OE devices and characterization of their basic performance. The 19-gauge needle–compatible miniaturized OE sensor has been successfully developed for a proof-of-concept study of pancreatic cancer detection. Basic electrical and optical performance of the assembled OE sensor has been characterized. (**A**) The handheld sensor module consists of a 19-gauge needle and a fabricated μPCB, which the OE components are assembled on. The μPCB is connected to another large-scale PCB to provide electrical connection to the control electronics. (**B**) Photo of the sensor module held by hand (**C**) size comparison with a U.S. dime. (**D**) A zoomed-in photo (scale bar, 1 mm) displays one type of the sensing unit, consisting of one phototransistor and three LEDs that are shown through a side-cut window of the hollow needle (internal diameter, 850 μm) in the commercial EUS-FNA unit. (**E** to **G**) LED light emission from different types of the fabricated sensors. (E) Single-unit type 1: 460- and 650-nm LEDs located on either side of a single phototransistor; (F) single-unit type 2: 460-nm LED located on one side, and 650-nm LED and NIR LED located on the other side of a single phototransistor; (G) dual unit: two single units (type 1) with a distance of ~5 mm between two phototransistors. (**H**) Forward voltage versus forward current curves of three assembled LEDs ($n = 5$ for 460- and 650-nm LEDs and $n = 1$ for 785-nm LED) (**I**) Linear relationship between forward current and optical power of three assembled LEDs. (**J**) Emission wavelengths of three LEDs measured by spectrophotometer. (**K**) The voltage detected by the phototransistor under constant LED power increases with the increase of the scatterer [Intralipid (IL)] concentrations for both the blue and red LEDs. The error bars represent SDs. Photo credit: Seung Yup Lee and Brandon Baier, University of Michigan.

FNA needle (ECHO-HD-19-C, Cook Medical), and the connecting PCB for electrical connection to the custom control electronics and space to be held by finger (Fig. 3B). Figure 3D displays a zoomed-in image of the sensor assembly inside the needle. Depending on the number of LEDs and the number of sensing units, a variety of design configurations is feasible, including a basic sensing unit with 460- and 650-nm LEDs (Fig. 3E), an advanced unit with additional near-infrared (NIR; 785 nm) LED (Fig.3F), and a dual-unit module that aligns two sub-single units (Fig. 3G). For demonstration purpose, all of the sensors shown here are imaged before the epoxy encapsulation process, which is the final step to provide a transparent protective window for the sensor. Further details on the fabrication and assembly process are described in Materials and Methods, and a step-by-step recipe can be found in notes S1 and S2 and fig. S2.

Electrical and optical characterization

The electrical and optical properties of the LED and phototransistor assembled onto the fabricated μPCB were evaluated. Figure 3H shows I_f (forward current)–V_f (forward voltage) characteristic curves of each LED. The measured optical powers from each LED are linear to the input forward current (Fig. 3I). To assess the effectiveness of the LED assembly, we measured a well-plug efficiency, defined as output optical power divided by input electrical power, of 21.7 ± 2.9% (for 460 nm, ±SD), 21.2 ± 4.2% (for 650 nm), and 22.1% (for 785 nm). The measured peak wavelengths by spectrometer are 458 ± 15 nm (peak ± full width at half maximum), 644 ± 15 nm, and 783 ± 18 nm (Fig. 3J). The performance of the assembled phototransistors was indirectly evaluated by measuring the detection voltage under conditions of constant LED output onto a tissue-simulating phantom with increasing concentrations of 20% Intralipid (scattering agent). The detection voltage reading increases as the concentration increases (Fig. 3K).

Tissue-simulating liquid phantom study

The optical sensing capability was evaluated using a set of tissue-simulating liquid phantoms. The phantoms were mixtures of deionized water and microspheres (scattering agent) titrated with a hemoglobin powder in increments of 5 μM (Fig. 4A) to alter the reflectance spectrum (Fig. 4B). Each phantom was measured by both our developed OE system using one single-unit sensor (Fig. 2E), one dual-unit sensor (Fig. 2G), and our fiber optic–based DRS system (*12*, *16*). Figure 4B displays the measured reflectance spectra from each phantom (solid lines) and the measured reflectance by the OE system using a single-unit sensor at 460 and 650 nm (diamond makers), indicating excellent agreement between the two devices. When the hemoglobin concentration increases from 10 to 40 μM, R_{450} decreases by ~30%, while R_{650} stays consistent. The R_{460}/R_{650} measured by three independent sensing units agrees well with DRS-measured R_{460}/R_{650} on each phantom as shown in Fig. 4C. Despite slight differences in absolute R_{460}/R_{650} between the different sensing units, OE-measured R_{460}/R_{650} shows a linear correlation with the DRS

measurements (Pearson's correlation = 0.96; Fig. 4D). The measured SNRs are 55.92 ± 2.07 and 55.98 ± 3.61 dB for 460 and 650 nm, respectively. There was no observed breakdown or performance degradation of the fabricated sensor after submersion into the liquid phantom, which demonstrates water resistance.

Ex vivo human pilot study

Last, we validated the developed OE sensor prototypes on freshly excised human pancreatic tissues during pancreatic surgery (four patients and 48 sites: 20 PDAC, 18 CP, 2 adipose tissue, and 8 normal pancreas), as shown in Fig. 5, A to C. To acquire site-matched biopsies for the gold standard histology, the dual-unit sensor (Fig. 3G) without the FNA needle was placed on the surface of the pancreatic tissues. One placement of the dual-unit sensor sequentially measured two sites. Multiple (four to seven times) placements were made for each pancreas. No physical damage to the measured tissue sites was observed during histopathological analysis, confirming the safety of optical sensing. Among the 48 measured sites, 8 sites (1 normal, 3 CP, and 4 PDAC) were excluded on the basis of our predetermined criteria considering blood contamination, bad contact between tissue and sensor, or motion artifacts. Two sites were adipose tissues of no interest in this study.

Figure 5D shows the measured reflectance ratios by one of the subunits on the individual sites from all four patients. The R_{460}/R_{650} of PDAC (red) is consistent (0.59 to 0.84) across three different

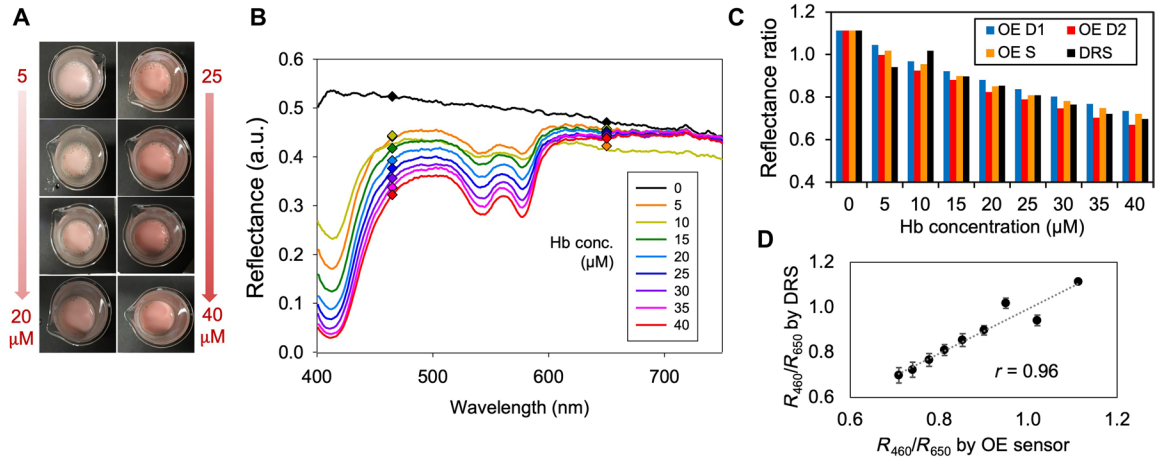

Fig. 4. Results of the bench-top experiments with tissue-simulating phantom. (**A**) The developed OE sensing system has been verified using a set of liquid phantoms with varying hemoglobin concentrations ([HbT]) in comparison with our DRS system. (**B**) The measured relative reflectance at both wavelengths by DRS (solid lines) and the OE sensing system (diamond markers) are comparable across the different [HbT]. a.u., arbitrary units. (**C**) The reflectance ratios R_{460}/R_{650} decrease as [HbT] increases in all of three single sensing units: Two units (OE D1 and OE D2) are from the same dual-unit sensor; the third one (OE S) is from a single-unit sensor. (**D**) The averaged R_{460}/R_{650} measured by three OE units and DRS-measured R_{460}/R_{650} are linearly correlated (Pearson's correlation $r = 0.96$). Error bars represent SDs of the values from three units. Photo credit: Seung Yup Lee, University of Michigan.

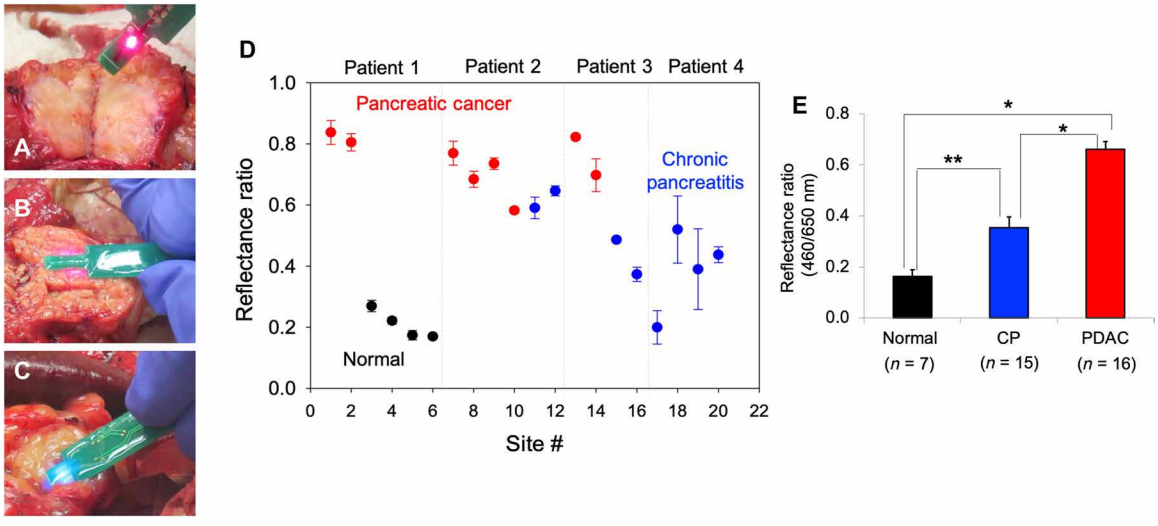

Fig. 5. Results of the pilot study on human tissues. The developed OE sensing system has been validated in ex vivo measurements on resected human pancreas (a total of four patients and 48 sites) during pancreatic surgery. The freshly excised human pancreas is measured by our fabricated dual-sensing-unit OE probe [(**A**) pancreatic cancer; (**B**) normal; (**C**) CP]. (**D**) Scatter plot of reflectance ratios (R_{460}/R_{650}) acquired using the subunit 1 from all the sites and all the patients. (**E**) The differences in the measured reflectance ratios R_{460}/R_{650} between normal, CP, and PDAC are statistically significant (*$P < 0.001$ and **$P = 0.007$, Wilcoxon rank sum test). The error bars represent SEs. Photo credit: Seung Yup Lee, University of Michigan.

patients, clearly distinguished from the normal pancreas sites (black, 0.17 to 0.27). The R_{460}/R_{650} of CP is between that of PDAC and normal tissues with a relatively higher variation. Figure 5E displays the averaged R_{460}/R_{650} of all sites of three tissue types, demonstrating that the reflectance ratios can significantly differentiate three pancreatic tissue types. Moreover, the OE-measured R_{460}/R_{650} of each tissue type is comparable with the DRS-measured R_{460}/R_{650} (normal, 0.163 ± 0.027 versus 0.315 ± 0.013; CP, 0.355 ± 0.041 versus 0.430 ± 0.133; and PDAC, 0.661 ± 0.031 versus 0.690 ± 0.029; mean ± SE). The measured R_{460}/R_{650} per tissue type is slightly different between two sensing units (subunits 1 and 2) but not substantial, as shown in fig. S3.

DISCUSSION

We have proposed an optical sensing technique based on OE chips to overcome the low sampling area in pancreas that the needle-based fiber-optic spectroscopy can interrogate. The lateral alignment of multiple sensing units (a pair of source and detector) can assess multiple pancreatic tissue sites simultaneously throughout the side-cut window of the FNA needle. To achieve an ultraminiaturized form factor of the sensing unit beyond the limit of conventional techniques (i.e., soldering the packaged chips onto a PCB), unpackaged OE chips have been directly bonded onto the microfabricated PCB. Optical and thermal simulations have confirmed the feasibility of optical sensing (SNR and capability to differentiate pancreatic tissue types) and thermal stability. The integrated sensing system (microprobe + custom electronics + GUI) has been verified in tissue-simulating phantoms and further validated on freshly excised human pancreatic tissues. Table S1 summarizes the overall engineering specification of the developed system, demonstrating the potential of rapid, multisite, and quantitative pancreatic tissue assessments in comparison with our group's trimodal optical spectroscopy system called the reflectance and fluorescence lifetime spectrometer (RFLS). Despite the tremendous reduction of footprint (l000-fold smaller) and power consumption (100-fold lower), our OE system holds promise to replace our cart-held RFLS. This is further supported by our recent study (*8*) finding that only reflectance spectroscopy has a comparable diagnostic performance with combined reflectance and fluorescence spectroscopy.

The apparent difference in the OE-measured reflectance ratio (R_{460}/R_{650}) between three pancreatic tissue types is consistent with our previous ex vivo human studies measuring a full reflectance spectrum (420 to 750 nm) of pancreatic tissues (*8*). Using a semiempirical analytical model, these studies have revealed that distinctive spectral features are associated with changes in the wavelength dependence of scattering by morphological alteration during tumor progression such as nuclear enlargement or stromal reaction with increases of collagen contents (*16*, *17*). Nuclei and collagen are two of the major light scatterers inside tissues, and their size and density are known to considerably affect the spectral scattering patterns (*18*–*21*). On the basis of our full spectrum dataset, there exists a number of other discrete wavelengths that could serve as valuable alternatives for our OE sensor. For example, the NIR regions (690 to 750 nm) enable deeper penetration into tissues due to substantially lower hemoglobin absorption. Moreover, the rate of reduced reflectance beyond 650 nm may provide an additional metric to differentiate cancerous tissues, as the slope of decreasing reflectance between 650 to 760 nm is different in Fig. 1B. These possibilities motivate the integration of the NIR LED into our sensor as a technical demonstration, although we did not perform any validation using this version of the sensor.

The key limitations of our study are design limitations necessary for this early-stage technical demonstration, ex vivo validation, and low patient number. Thus, this work should be considered to be a pilot study to demonstrate a proof-of-concept OE sensor that fits through a 19-gauge needle. Although the excised pancreatic tissues would not reflect a completely intact tissue environment (due to loss of blood vessels), site-level histopathology can serve as a gold standard for validation of our OE sensor. During our measurements on resected pancreas, the sensor readout was sensitive to unreliable contact between sensor and tissues and motion artifacts due to manual holding, resulting in the exclusion of ~15% of the obtained data. However, this issue is less of a concern for real clinical applications because our sensor will be inserted into bulk pancreatic tissues. Once the needle is inserted, the OE sensing window will be surrounded by soft pancreas, forming a solid, stationary contact whose motion can be controlled by clinicians operating the EUS-FNA. The real-time display of reflectance ratio can provide an indicator of good contact. Our ex vivo dataset can serve as a guideline of a normal range of the ratios.

For in situ assessment of pancreatic tissue during the EUS-FNA procedure, our next step is to implement an electrical connection through a 1-m-long FNA channel. Before in situ testing, it will also be important to ensure the mechanical integrity of the sensor given that the OE sensor will be subject to a bending deformation while the EUS probe is being delivered to the duodenum or stomach. The anticipated maximum bending angle that the OE sensor undergoes would be around 30° when it comes out of the EUS probe (fig. S4A). Although our initial testing on a silicon substrate on a bare stylet has confirmed its ability to endure that bending angle (fig. S4B), we will perform a more relevant bench-top testing using the commercial EUS endoscopy, EUS-FNA device, and a biologic endoscopy simulator (*22*). Last, we will extend our study on the precursor lesions of PDAC such as pancreatic mucinous cysts for early diagnosis that would significantly enhance the patient outcomes and management guidance. Our preliminary study on intraductal papillary mucinous neoplasm (IPMN), a precancerous neoplasm type that can progress to PDAC, has exhibited that the IPMN shares similar reflectance spectral features with PDAC (*17*).

The main technical challenges when fabricating the OE sensor include (i) establishing an optimal thermal profile for a eutectic-bonding process of two different types of LEDs, (ii) manual alignment of the LEDs and phototransistor onto the pads of the μPCB before the bonding process, and (iii) manual epoxy encapsulation. Instead of carrying out the thermal bonding process via an annealing tool, a flip chip bonder can be used for more precise bonding in the future. The manual epoxy packaging process may contribute to the slight differences in the measured R_{460nm}/R_{650nm} between each engineered sensing unit (fig. S2P) because it is hard to control the formed curvature of the ultraviolet (UV)–curable epoxy droplet on top of each LED and phototransistor. This curvature can affect LED emission or detection angle of the phototransistor, which can alter photon travel paths determining the degree of light attenuation by absorption like the numerical aperture effect for the fiber optic–based DRS (*23*).

Compared to the traditional fiber-based light sensing in biological tissues, OE-based sensing has multiple advantages summarized in table S4. First of all, the OE-based technique has huge flexibility

in the geometric configuration of the source and detector. For example, source-detection separation, which is critical for determining SNR, interrogation depth, and dependence with phase function in DRS analysis (*24*), is limited in the applications where the sites of interest require a very confined channel to access. A small single or dual fiber (<200-μm core size) for the source and detector with a small fiber can fit through the channel; however, these could suffer from a low SNR or too-shallow penetration depth. Another advantage of the OE-based technique is a high SNR. Since light emission and detection occur at the measuring sites for the OE sensors, there might be less optical loss compared to using optical fibers to and from a remote source and detector, which require a coupling scheme between optics and fibers (*25*). In this way, our fabricated OE sensor produces a comparable SNR without bulky and expensive high-end detectors such as a photomultiplier tube or an intensified charge-coupled device usually used in a fiber optic–based spectroscopy system. Moreover, the sensing unit's miniaturized footprint (<1.5 mm by 1.5 mm) can become a modular platform unit adaptable to many applications. For hollow-needle compatibility, this approach can be readily applied to other organs such as the liver and the lung (*26*), in which fiber optic–based spectroscopy has already been attempted. Coupled with the recent advances in flexible electronics (*27*), the OE sensing unit can be extended to two-dimensional mapping in a wearable device (*28*) or used as an implantable sensor (*29*). Wireless communication can be readily implemented on the converted electrical signals through near-field communication technology (*30*, *31*). The extremely light weight of the OE sensor can also avoid the significant distortion of reflectance and fluorescence spectra measured on soft biological tissues due to pressure effects (*32*, *33*) on the fiber-optic probes typically held by the operator's hands. However, the current biggest hurdle for widespread use of the OE approach is that more advanced optical sensing techniques, such as full-spectrum DRS or fluorescence spectroscopy and frequency- or time-domain sensing are limited because of scarcity of adequate miniaturized OE components. So far, only simple techniques based on continuous intensity monitoring such as pulse oximetry (*31*), continuous-wave NIR spectroscopy, and four-color spectroscopy (*30*) have been demonstrated. Moreover, temperature management and hermetic sealing of the OE sensor is more critical than for the fiber-optic probe, which is inherently inert to biological tissues. The ongoing technical innovation in materials, optoelectronics, and microfabrication with computational power will enable the development of various OE sensing techniques for biomedical applications (*34*).

In summary, we have successfully designed, engineered, and validated a proof-of-concept miniaturized OE sensor that is compatible with a 19-gauge FNA needle for rapid, volumetric, and quantitative assessment of pancreatic tissue. The prototyped device has shown comparable optical sensing performance with a conventional DRS system and the potential to distinguish pancreatic cancer from benign tissues. This fiber-less optical sensing technology in an ultraminiaturized form factor is highly configurable in terms of source-detection geometry and, thereby, can serve as a platform technology for a variety of light-based sensing techniques in biological tissues.

MATERIALS AND METHODS

Optical simulation: Zemax

The embedded MC function in the Zemax nonsequential mode was used to simulate photon propagation and detection by the LEDs and phototransistor in pancreatic tissues. LEDs (460 and 650 nm) were modeled as rectangular sources featured by their angular emission distributions and optical powers. The active area of the phototransistor was also modeled as a rectangular detector. For simulation simplicity, angular responsivity was not implemented; thus, any launched photons hitting the detection area were read in their total weights. All geometrical dimensions used (size of chips and source-detector separation) were consistent with the physical realization. The samples (i.e., pancreatic tissues) were modeled as a big cube (10 cm by 10 cm by 100 cm, width by depth by height) to ensure a semifinite medium. The optical properties of three pancreatic tissues (normal, CP, and PDAC) were input into the Zemax bulk scattering mode using a mean free path length and transmission. Both parameters were computed from the estimated wavelength-resolved absorption (μ_a) and scattering (μ_s) coefficients in our previous study using a semiempirical analysis model in human pancreatic tissues (see the parameters used in table S2) (*16*). To computationally explore the effect of temperature change on the OE sensor performance, we used μ_a and μ_s at 465 and 655 nm under the assumption of a 50°C increase because the LED emission wavelength roughly increases at 0.1 nm/°C (*15*). Although the forward voltage of the LED is known to decrease with increasing temperature (*35*), this effect was not included because our LED operated with a constant-current driver. The temperature dependence of the phototransistor was also not considered under the assumption that the ratiometric approach would cancel out that effect. The Henyey-Greenstein phase function was selected for scattering direction, and anisotropy was fixed to 0.9 to mimic highly forward scattering in biological tissues. For each simulation, a total of 100 million photons were launched to ensure a high SNR.

Thermal simulation: Ansys

A human pancreatic head was modeled as a cube with an edge of 3 cm. For the sensor assembly, two LEDs were simulated 1.2 mm apart from each other on a 150-μm-thick silicon wafer that was attached onto a steel stylet shaped in a half cylinder (Fig. 2B). The properties related to heat transfer, including heat capacity, density, and thermal conductivity, of the pancreatic head, silicon wafer, and steel stylet were inputs to the model for both steady-state and time-transient simulations (table S3). Because of the symmetrical structure of the model, the simulation was performed only on one-half of the model. Around 230,000 nodes were used to analyze this model. Finer-sized elements were meshed around the LEDs and the silicon wafer because significant temperature variations exist in these areas. The power due to heat was determined by equating it to the electrical power of 10 mW, which is the power necessary to emit the required optical power of ~1 mW, estimated from the previous optical simulations. The initial temperature of the pancreas was set to 36.5°C.

Fabrication and assembly

Our μPCB (30 mm by 0.7 mm by 0.15 mm, width by length by thickness) was fabricated on a silicon wafer with 500-μm thickness (2-μm-thick oxide layer on top for insulation) following a well-established "Michigan probe" microfabrication technology (*36*, *37*). Each step of the fabrication and assembly is listed in notes S1 and S2 and illustrated in fig. S2. Briefly, Ti/Pt/Au and Au/In layers were patterned by lift-off process for the bottom pad contacts of the LED and phototransistor and interconnections to external pads for the connecting PCB board (Fig. 3A). The unpackaged LEDs and phototransistor

were bonded onto this fabricated μPCB via two sequential eutectic bonding processes to attach with the bottom electrodes of the LEDs and phototransistors (fig. S2, M and N). Then, wire bonding followed to connect the top electrodes of those components with the pads on the μPCB (fig. S2O). Given the size of the μPCB (widths between interconnections and pads) and die-level components, all bonding processes were performed within ±20-μm precision. The UV-cured transparent epoxy encapsulated the sensor assembly for protection. Each pad at the other end of the μPCB was connected to the connecting PCB via additional wire bonding (Fig. 3A). These bonded wires were enclosed with the same UV-cured epoxy, and Omnetics connectors (A79002-001 and A79005-001, Omnetics Connector Corporation, Minneapolis, MN) were used for electrical interfacing with external control electronics.

Custom electronics and GUI program

Custom control electronics were designed and developed to drive two LEDs and read the detection signals from the phototransistor via the TIA. The microcontroller based on a 32-bit ARM core (ST32F405OE, STMicroelectronics, Geneva, Switzerland) was the central unit to control the illumination sequence of two LEDs, set the gains on a programmable gain amplifier (PGA), read the analog-to-digital converted voltage values from the TIA coupled with PGA, and send this voltage data to a remote laptop computer via USB connection for data processing and storage. The low-noise LED current driver was implemented using a digital-to-analog converter (AD5452, Analog Device, Norwood, MA). The TIA was designed to convert the phototransistor current to a voltage signal with amplification of 10^5 and first-order low-pass filtering with a cutoff frequency of 1 kHz. The PGA (LTC6910, Linear Technology, Milpitas, CA) enabled additional gain adjustment through digital control, providing a high dynamic range. The amplified voltage was subsequently filtered for a high SNR. The 16-bit analog-digital converter (ADS1115, Texas Instruments, Dallas, TX) read the resulting voltages at 50 kHz. The GUI program was written in C# to provide user input operation, display, and save the voltage data.

Calibration and data processing

The corrected reflectance (R_{corr}) was obtained from a calibration process represented by Eq. 1. The reflectance intensities (R_{meas_sample}) measured by our OE sensor were subtracted by the baseline measurements (R_{meas_water}) and corrected for the system spectral response characterized by measuring a calibration phantom (R_{meas_std}) with known reflectivity (r_{std}). Because of an extremely small gap between the LED and phototransistor, manual epoxy encapsulation covered all components together (fig. S2P), which caused phototransistor readings without sample measurements via either direct LED light incidence or total internal reflection at the interface between epoxy and air. These default baseline readings were measured in water because water provided a close refractive index to biological tissues (n = 1.33) but no scattering. The calibrating liquid phantom was prepared every time before our measurement using 1-μm-sized polystyrene microsphere (07310-15, Polysciences, Warrington, PA) in deionized water. Its reflectivity (r_{std}) was estimated using our fiber optic–based DRS system coupled with the Spectralon diffuse reflectance standard (SRS-99-020, Labsphere, North Sutton, NH). The measured reflectance of this liquid calibration phantom by our sensor (R_{meas_std}) was also baseline-subtracted and used as a scaling factor to address the spectral response of the system. Then, the reflectance ratio is calculated on corrected reflectance at both wavelengths by $R_{corr\_460nm}/R_{corr\_650nm}$

$$R_{corr} = \frac{R_{meas\_sample} - R_{meas\_water}}{R_{meas\_std} - R_{meas\_water}} \times r_{std} \quad (1)$$

Phantom experiments

The set of tissue-simulating liquid phantoms was made by titrating 5 μM hemoglobin (H0267, Sigma-Aldrich, St. Louis, MO) to a base in which a predetermined concentration of 1-μm-sized polystyrene microspheres was mixed with deionized water (30 ml) to mimic the reduced scattering coefficient of human pancreatic tissues (~10 cm^{-1}). The fabricated sensing modules (one single unit and one dual unit) were submerged in the phantom while ensuring that the sensing unit was located in the middle of the beaker. As a reference reading, our DRS system also measured each phantom using the fiber-optic probe with a source-detector separation of 660 μm. Details on DRS acquisition, calibration, and analysis can be found in several of our previous studies (*12*, *16*). Each phantom was measured three times using both devices. The SNR of the OE sensors was quantified by 20 $\log_{10}(\sigma(I)/\mu(I))$ dB. Here, $\mu(I)$ represents the average of 20 data points in one acquisition and $\sigma(I)$ is the SD. The representative SNRs for 460 and 650 nm were averaged out across three sensing units, three repetitions, and all phantoms.

Ex vivo human tissue measurements

For pilot validation in human tissues, we measured on the resected pancreas during the operative procedure (Whipple or distal pancreatectomy) in a total of four patients. The study was approved by the Institutional Review Board of the University of Michigan School of Medicine. Written consent was acquired from each patient before surgery. The resected portion of pancreas during the surgery was immediately transferred to the gross room. The pathologists cleaned excess blood from tissue and cut open the sites of interest for optical sensing. Our prototyped dual-unit sensor without the FNA needle was placed on the surface of the tissue and held by the operator's hands. The acquisition time was less than 1 s, and three repetitions were made per site. Immediately after OE data acquisition, the measured tissue sites were extracted in a rectangular shape with a size of 1 cm by 0.5 cm for gold standard histopathological analysis. The shorter edge of a cut sample was marked with black ink to label the site where the subunit 1 measured. All measurements were completed within 1 hour after resection. Any site with the measured R_{460}/R_{650} lower than 0.01 and SNR < 20 dB was excluded from analysis because of excessive blood, motion artifact, or measurement errors.

Statistical analysis

The difference in optical data between the different pancreatic tissue types in the human study was analyzed using Wilcoxon rank sum tests, and statistical significance was assessed at the 0.05 level. All statistical tests (Pearson correlation and Wilcoxon rank sum tests) were conducted using the R statistical package (version 3.4.1, R Foundation).

SUPPLEMENTARY MATERIALS

Supplementary material for this article is available at http://advances.sciencemag.org/cgi/content/full/6/47/eabc1746/DC1

View/request a protocol for this paper from *Bio-protocol*.

REFERENCES AND NOTES

1. Cancer Facts & Figures 2019, American Cancer Society; www.cancer.org/research/cancer-facts-statistics/all-cancer-facts-figures/cancer-facts-figures-2019.html.
2. L. Rahib, B. D. Smith, R. Aizenberg, A. B. Rosenzweig, J. M. Fleshman, L. M. Matrisian, Projecting cancer incidence and deaths to 2030: The unexpected burden of thyroid, liver, and pancreas cancers in the United States. *Cancer Res.* **74**, 2913–2921 (2014).
3. L. Zhang, S. Sanagapalli, A. Stoita, Challenges in diagnosis of pancreatic cancer. *World J. Gastroenterol.* **24**, 2047–2060 (2018).
4. S. Varadarajulu, A. Tamhane, M. A. Eloubeidi, Yield of EUS-guided FNA of pancreatic masses in the presence or the absence of chronic pancreatitis. *Gastrointest. Endosc.* **62**, 728–736 (2005).
5. P. Kedia, M. Gaidhane, M. Kahaleh, Technical advances in endoscopic ultrasound (EUS)-guided tissue acquisition for pancreatic cancers: How can we get the best results with EUS-guided fine needle aspiration? *Clin. Endosc.* **46**, 552–562 (2013).
6. M. Chandra, J. Scheiman, D. Simeone, B. McKenna, J. Purdy, M.-A. Mycek, Spectral areas and ratios classifier algorithm for pancreatic tissue classification using optical spectroscopy. *J. Biomed. Opt.* **15**, 010514 (2010).
7. R. H. Wilson, M. Chandra, L.-C. Chen, W. R. Lloyd, J. Scheiman, D. Simeone, J. Purdy, B. McKenna, M.-A. Mycek, Photon-tissue interaction model enables quantitative optical analysis of human pancreatic tissues. *Opt. Express* **18**, 21612–21621 (2010).
8. R. H. Wilson, M. Chandra, J. M. Scheiman, S. Y. Lee, O. E. Lee, B. J. McKenna, D. M. Simeone, J. M. G. Taylor, M.-A. Mycek, Tissue classification using optical spectroscopy accurately differentiates cancer and chronic pancreatitis. *Pancreas* **46**, 244–251 (2017).
9. W. R. Lloyd, R. H. Wilson, S. Y. Lee, M. Chandra, B. McKenna, D. Simeone, J. Scheiman, M.-A. Mycek, In vivo optical spectroscopy for improved detection of pancreatic adenocarcinoma: A feasibility study. *Biomed. Opt. Express* **5**, 9–15 (2014).
10. P. L. Stegehuis, L. S. F. Boogerd, A. Inderson, R. A. Veenendaal, P. van Gerven, B. A. Bonsing, J. S. Mieog, A. Amelink, M. Veselic, H. Morreau, C. J. H. van de Velde, B. P. F. Lelieveldt, J. Dijkstra, D. J. Robinson, A. L. Vahrmeijer, Toward optical guidance during endoscopic ultrasound-guided fine needle aspirations of pancreatic masses using single fiber reflectance spectroscopy: A feasibility study. *J. Biomed. Opt.* **22**, 024001 (2017).
11. L. Zhang, D. K. Pleskow, V. Turzhitsky, E. U. Yee, T. M. Berzin, M. Sawhney, S. Shinagare, E. Vitkin, Y. Zakharov, U. Khan, F. Wang, J. D. Goldsmith, S. Goldberg, R. Chuttani, I. Itzkan, L. Qiu, L. T. Perelman, Light scattering spectroscopy identifies the malignant potential of pancreatic cysts during endoscopy. *Nat. Biomed. Eng.* **1**, 0040 (2017).
12. M. Chandra, J. Scheiman, D. Heidt, D. Simeone, B. McKenna, M.-A. Mycek, Probing pancreatic disease using tissue optical spectroscopy. *J. Biomed. Opt.* **12**, 060501 (2007).
13. C. M. Lochner, Y. Khan, A. Pierre, A. C. Arias, All-organic optoelectronic sensor for pulse oximetry. *Nat. Commun.* **5**, 5745 (2014).
14. S. Y. Lee, Y. G. Chung, M.-A. Mycek, In situ optical tissue diagnostics/miniaturized optoelectronic sensors for tissue diagnostics, in *Encyclopedia of Modern Optics*, B. D. Guenther, D. G. Steel, Eds. (Elsevier, ed. 2, 2018), pp. 86–94.
15. K. J. Reynolds, J. P. de Kock, L. Tarassenko, J. T. B. Moyle, Temperature dependence of LED and its theoretical effect on pulse oximetry. *Br. J. Anaesth.* **67**, 638–643 (1991).
16. R. H. Wilson, M. Chandra, J. Scheiman, D. Simeone, B. McKenna, J. Purdy, M.-A. Mycek, Optical spectroscopy detects histological hallmarks of pancreatic cancer. *Opt. Express* **17**, 17502–17516 (2009).
17. S. Y. Lee, W. R. Lloyd, M. Chandra, R. H. Wilson, B. McKenna, D. Simeone, J. Scheiman, M.-A. Mycek, Characterizing human pancreatic cancer precursor using quantitative tissue optical spectroscopy. *Biomed. Opt. Express* **4**, 2828–2834 (2013).
18. L. T. Perelman, V. Backman, M. Wallace, G. Zonios, R. Manoharan, A. Nusrat, S. Shields, M. Seiler, C. Lima, T. Hamano, I. Itzkan, J. Van Dam, J. M. Crawford, M. S. Feld, Observation of periodic fine structure in reflectance from biological tissue: A new technique for measuring nuclear size distribution. *Phys. Rev. Lett.* **80**, 627–630 (1998).
19. J. R. Mourant, M. Canpolat, C. Brocker, O. Esponda-Ramos, T. M. Johnson, A. Matanock, K. Stetter, J. P. Freyer, Light scattering from cells: The contribution of the nucleus and the effects of proliferative status. *J. Biomed. Opt.* **5**, 131–137 (2000).
20. I. S. Saidi, S. L. Jacques, F. K. Tittel, Mie and Rayleigh modeling of visible-light scattering in neonatal skin. *Appl. Optics* **34**, 7410–7418 (1995).
21. D. Arifler, I. Pavlova, A. Gillenwater, R. Richards-Kortum, Light scattering from collagen fiber networks: Micro-optical properties of normal and neoplastic stroma. *Biophys. J.* **92**, 3260–3274 (2007).
22. J. Hochberger, K. Matthes, J. Maiss, C. Koebnick, E. G. Hahn, J. Cohen, Training with the compactEASIE biologic endoscopy simulator significantly improves hemostatic technical skill of gastroenterology fellows: A randomized controlled comparison with clinical endoscopy training alone. *Gastrointest. Endosc.* **61**, 204–215 (2005).
23. A. M. J. Wang, J. E. Bender, J. Pfefer, U. Utzinger, R. A. Drezek, Depth-sensitive reflectance measurements using obliquely oriented fiber probes. *J. Biomed. Opt.* **10**, 44017 (2005).
24. K. W. Calabro, I. J. Bigio, Influence of the phase function in generalized diffuse reflectance models: Review of current formalisms and novel observations. *J. Biomed. Opt.* **19**, 075005 (2014).
25. K. Vishwanath, K. Chang, D. Klein, Y. F. Deng, V. Chang, J. E. Phelps, N. Ramanujam, Portable, fiber-based, diffuse reflection spectroscopy (DRS) systems for estimating tissue optical properties. *Appl. Spectrosc.* **65**, 206–215 (2011).
26. S. C. Kanick, C. van der Leest, R. S. Djamin, A. M. Janssens, H. C. Hoogsteden, H. J. C. M. Sterenborg, A. Amelink, J. G. J. V. Aerts, Characterization of mediastinal lymph node physiology in vivo by optical spectroscopy during endoscopic ultrasound-guided fine needle aspiration. *J. Thorac. Oncol.* **5**, 981–987 (2010).
27. S. Choi, H. Lee, R. Ghaffari, T. Hyeon, D.-H. Kim, Recent advances in flexible and stretchable bio-electronic devices integrated with nanomaterials. *Adv. Mater.* **28**, 4203–4218 (2016).
28. Y. Khan, D. Han, A. Pierre, J. Ting, X. Wang, C. M. Lochner, G. Bovo, N. Yaacobi-Gross, C. Newsome, R. Wilson, A. C. Arias, A flexible organic reflectance oximeter array. *Proc. Natl. Acad. Sci. U.S.A.* **115**, E11015–E11024 (2018).
29. H. Zhang, P. Gutruf, K. Meacham, M. C. Montana, X. Zhao, A. M. Chiarelli, A. Vázquez-Guardado, A. Norris, L. Lu, Q. Guo, C. Xu, Y. Wu, H. Zhao, X. Ning, W. Bai, I. Kandela, C. R. Haney, D. Chanda, R. W. Gereau IV, J. A. Rogers, Wireless, battery-free optoelectronic systems as subdermal implants for local tissue oximetry. *Sci. Adv.* **5**, eaaw0873 (2019).
30. J. Kim, G. A. Salvatore, H. Araki, A. M. Chiarelli, Z. Xie, A. Banks, X. Sheng, Y. Liu, J. W. Lee, K.-I. Jang, S. Y. Heo, K. Cho, H. Luo, B. Zimmerman, J. Kim, L. Yan, X. Feng, S. Xu, M. Fabiani, G. Gratton, Y. Huang, U. Paik, J. A. Rogers, Battery-free, stretchable optoelectronic systems for wireless optical characterization of the skin. *Sci. Adv.* **2**, e1600418 (2016).
31. J. Kim, P. Gutruf, A. M. Chiarelli, S. Y. Heo, K. Cho, Z. Xie, A. Banks, S. Han, K.-I. Jang, J. W. Lee, K.-T. Lee, X. Feng, Y. Huang, M. Fabiani, G. Gratton, U. Paik, J. A. Rogers, Miniaturized battery-free wireless systems for wearable pulse oximetry. *Adv. Funct. Mater.* **27**, 1604373 (2017).
32. Y. Ti, W.-C. Lin, Effects of probe contact pressure on in vivo optical spectroscopy. *Opt. Express* **16**, 4250–4262 (2008).
33. L. Lim, B. S. Nichols, N. Rajaram, J. W. Tunnell, Probe pressure effects on human skin diffuse reflectance and fluorescence spectroscopy measurements. *J. Biomed. Opt.* **16**, 011012 (2011).
34. S. H. Yun, S. J. J. Kwok, Light in diagnosis, therapy and surgery. *Nat. Biomed. Eng.* **1**, 0008 (2017).
35. D. S. Meyaard, J. Cho, E. Fred Schubert, S.-H. Han, M.-H. Kim, C. Sone, Analysis of the temperature dependence of the forward voltage characteristics of GaInN light-emitting diodes. *Appl. Phys. Lett.* **103**, 121103 (2013).
36. K. Najafi, K. D. Wise, An implantable multielectrode array with on-chip signal processing. *IEEE J. Solid State Circuits* **21**, 1035–1044 (1986).
37. K. D. Wise, D. J. Anderson, J. F. Hetke, D. R. Kipke, K. Najafi, Wireless implantable microsystems: High-density electronic interfaces to the nervous system. *Proc. IEEE* **92**, 76–97 (2004).

Acknowledgments: We thank W. Lloyd and F. Wu for discussions on early concept design. We also thank multiple colleagues for technical support including K. Kampasi for eutectic bonding, J. K. Woo for wire bonding, I. Shin and G. Cheon for the control electronics and GUI program, and J. Ahn for thermal simulation. Last, we appreciate R. Goff for clinical coordination. **Funding:** This research was supported by the NIH (R21-EB018537), University of Michigan (UM) Comprehensive Cancer Center, UM Rackham Research Fund, and UM Lurie Nanofabrication Facility (LNF). **Author contributions:** S.Y.L., J.M.S., E.Y., B.J.M., D.M.S., and M.-A.M. designed the study. S.Y.L., J.M.P., and K.N. designed and fabricated the device. S.Y.L. and J.M.P. performed in vitro experiments. D.M.S. facilitated patient recruitment. S.Y.L, J.M.P., J.S., and B.J.M. conducted the human study. J.S. and B.J.M. performed histopathology. S.Y.L., J.M.S., and M.-A.M. analyzed and interpreted the data. S.Y.L., J.M.P., K.N., J.M.S., and M.-A.M. wrote the paper. All coauthors contributed to editing the paper. **Competing interests:** S.Y.L., E.Y., J.M.S., and M.-A.M. are inventors on a pending patent related to this work filed by the University of Michigan (no.15/706,900, filed on 18 September 2017, published on 11 January 2018). The authors declare no other competing interests. **Data and materials availability:** All data needed to evaluate the conclusions in the paper are present in the paper and/or the Supplementary Materials. Additional data related to this paper may be requested from the authors.

Submitted 17 April 2020
Accepted 7 October 2020
Published 20 November 2020
10.1126/sciadv.abc1746

Citation: S. Y. Lee, J. M. Pakela, K. Na, J. Shi, B. J. McKenna, D. M. Simeone, E. Yoon, J. M. Scheiman, M.-A. Mycek, Needle-compatible miniaturized optoelectronic sensor for pancreatic cancer detection. *Sci. Adv.* **6**, eabc1746 (2020).